SCIENCE CHINA
Earth Sciences

•RESEARCH PAPER•

January 2021 Vol.64 No.1: 110–126
https://doi.org/10.1007/s11430-019-9663-4

Quasi-waveform seismic tomography of crustal structures in the capital circle region of China

Xueyuan HUANG[1], Dinghui YANG[2*], Ping TONG[3,4], Yuan GAO[5], Yutao SHI[5] & Hao WU[2]

[1] *Department of Applied Statistics, School of Mathematics and Statistics, Beijing Technology and Business University, Beijing 100048, China;*
[2] *Department of Mathematical Sciences, Tsinghua University, Beijing 100084, China;*
[3] *Division of Mathematical Sciences, School of Physical and Mathematical Sciences, Nanyang Technological University, Singapore 637371, Singapore;*
[4] *Asian School of the Environment, Nanyang Technological University, Singapore 637371, Singapore;*
[5] *Institute of Earthquake Science, China Earthquake Administration, Beijing 100036, China*

Received November 24, 2019; revised June 10, 2020; accepted July 20, 2020; published online November 2, 2020

Abstract Seismic tomography is one of the main tools to explore the interior of the earth. In this study, the quasi-waveform seismic tomographic method is used for the first time to reveal the crustal structures in the capital region of China. 3-D high-resolution V_P, V_S and the Poisson's ratio models are generated by inverting 29839 direct P- and 29972 direct S-wave traveltimes selected from 3231 local earthquakes. The results reveal strong crustal heterogeneities. The velocity anomalies at shallow depths are well consistent with surface geologic structures. The relatively low-velocity anomaly layer in the middle crust may be the result of multiple phases of tectonic activity. Earthquakes generally occurred on the boundaries of high- and low-velocity and Poisson's ratio anomalies. There are obvious low-velocity anomalies below the hypocenters of the Tangshan earthquake and the historical Sanhe-Pinggu earthquake, implying the existence of fluids. The similar velocity structures around the hypocenters of the two earthquakes indicate that the occurrences of the two earthquakes may be related to the same mechanism. The high-resolution velocity models provide important observational constraints on the small-scale heterogeneities and dynamic mechanism of the crust in the capital region of China.

Keywords Quasi-waveform inversion, Capital circle region, Seismic tomography, Crustal velocity structure, Heterogeneity

Citation: Huang X, Yang D, Tong P, Gao Y, Shi Y, Wu H. 2021. Quasi-waveform seismic tomography of crustal structures in the capital circle region of China. Science China Earth Sciences, 64(1): 110–126, https://doi.org/10.1007/s11430-019-9663-4

1. Introduction

On May 26, 2020, an M3.6 earthquake with a focal depth of 18 km occurred in Mentougou, west of Beijing City. In April 2019, two earthquakes, with magnitudes 2.9 (on April 7 at a focal depth of 17 km) and 3.0 (on April 14 at a focal depth of 19 km), occurred in Haidian and Huairou, respectively. These earthquakes could be felt in most of the urban areas of Beijing. The earthquakes, especially the two earthquakes occurred just one week apart in 2019, drew public attention to the problems of seismic activity, preparation, and the underlying structures beneath Beijing and its surrounding areas. Beijing, as the capital of China with its developed economy and dense population, is an important political, economic and cultural center. Meanwhile, it is also one of the intraplate earthquake-prone regions in eastern China (Figure 1) (Jia et al., 2005; Huang, 2016). Beijing and its surrounding areas (the capital circle region) are located in the northern part of the North China Basin, with the Taihangshan Mountain and the Yanshan Mountain on its west and north and the Bohai Sea on its east (Qi et al., 2006). The northwest part of this region is seismically active due to the con-

---

* Corresponding author (email: ydh@tsinghua.edu.cn)

vergence of the Yinshan-Yanshan orogenic belt and the Ordos Block (Tian et al., 2009). In the Taihangshan Uplift area, which is along the boundary of the North China Basin and the Ordos Block, and the Yanshan Uplift area, the earthquakes are distributed in belts. Besides, the Tanlu fault zone stretches across the Bohai Sea on the east (Tian et al., 2009; Lv, 2009). The crustal thickness of the capital region changes greatly and is roughly thicker in the Northwest and thinner in the Southeast (Zhang, 1998; Li et al., 2001; Shi et al., 2014; Zhang et al., 2019). In a larger scale view, the capital region is located at the front of the boundary between the Eurasian Plate and the Pacific Plate. This complex geologic structure and the resulting frequent seismicity are a threat to economic development and human lives in this area.

Large earthquakes have struck the capital circle region frequently throughout history (as shown in Figure 1). For example, the *M*8.0 Sanhe-Pinggu earthquake, which occurred east of Beijing in 1679, was the largest earthquake in this region in recorded history (Zhang et al., 2002), while the *M*7.8 Tangshan earthquake that occurred in 1976 resulted in more than 242,000 deaths and 165,000 injuries. In addition to these large earthquakes, earthquakes with magnitudes of more than 5.0 occur occasionally, such as the *M*6.2 Zhangbei earthquake in 1998 and the *M*5.3 Wen'an earthquake in July 2006. The seismicity in this region is periodic (Ma et al., 2004), with a large number of small earthquakes occurring every year (Zhao et al., 2013).

From the perspective of the geologic setting (as shown in Figure 2), the North China Basin consists of a series of tectonic units, such as the Jizhong Depression, the Linqing Depression, the Cangxian Uplift, the Huanghua Depression and the Chengning Uplift, which are nearly parallel to the Taihangshan Front fault and the Taihangshan Uplift and are distributed from west to east with an NNE orientation (Lv, 2009; Huang and Zhao, 2004; Ye et al., 1985, 1987; Liu, 1987; Huang, 2016). The region includes several fault zones, such as the Taihangshan Front fault zone, the Cangxian fault zone, the Yuxian-Yanqing fault zone, and the Changli-Ninghe fault zone (Lv, 2009). The active faults are primarily distributed in the North China Basin and the Taihangshan Uplift region, which have NE orientations, while the Yanshan Uplift zone in the north with an E-W orientation is relatively stable (Huang and Zhao, 2009). The Zhangjiakou-Penglai seismic belt in NW-SE direction is seismically active zone, and most of the seismicity occurs in the belt; the Ninghe-Tangshan-Luanxian, Sanhe-Pinggu and Huailai-Yuxian zones, with NE-SW orientation, are also seismically active regions (Huang and Zhao, 2004; Zhao et al., 2013).

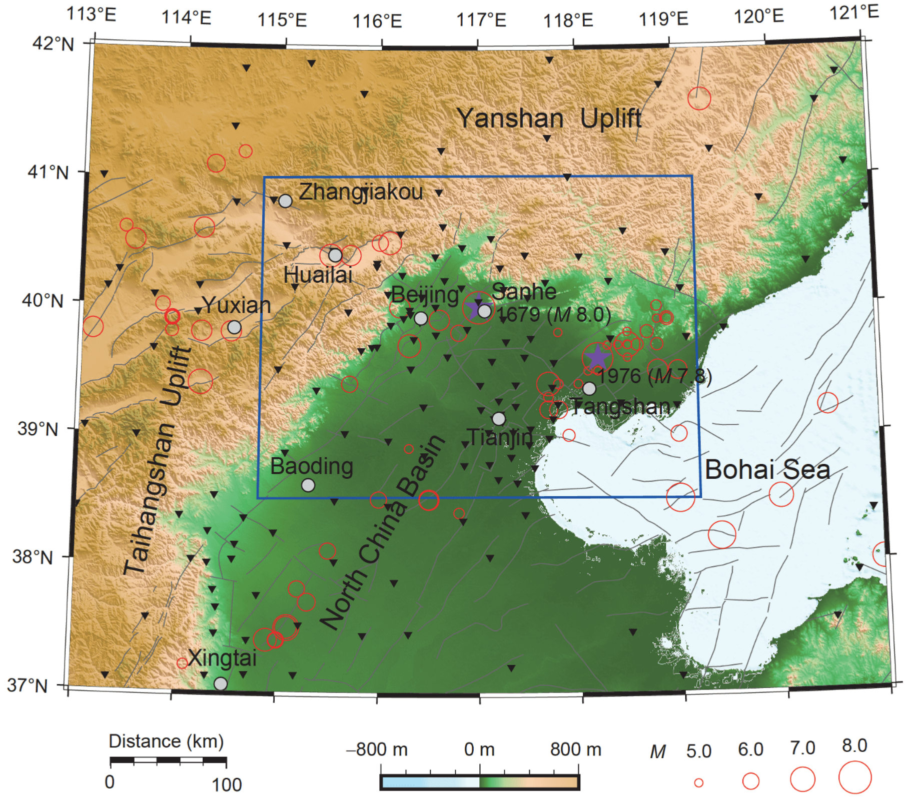

Figure 1 The tectonic background of the capital circle region. The blue box indicates the present study area. The open circles give the locations and sizes of the earthquakes larger than *M*5.0 since AD1500, and the two purple stars represent the Sanhe-Pinggu *M*8.0 earthquake that occurred in 1679 and the Tangshan *M*7.8 earthquake in 1976, respectively. The black reverse triangles show the spatial distribution of stations. Major faults are shown in the gray curves. The topography and the sizes of earthquakes are shown as legends at the bottom.

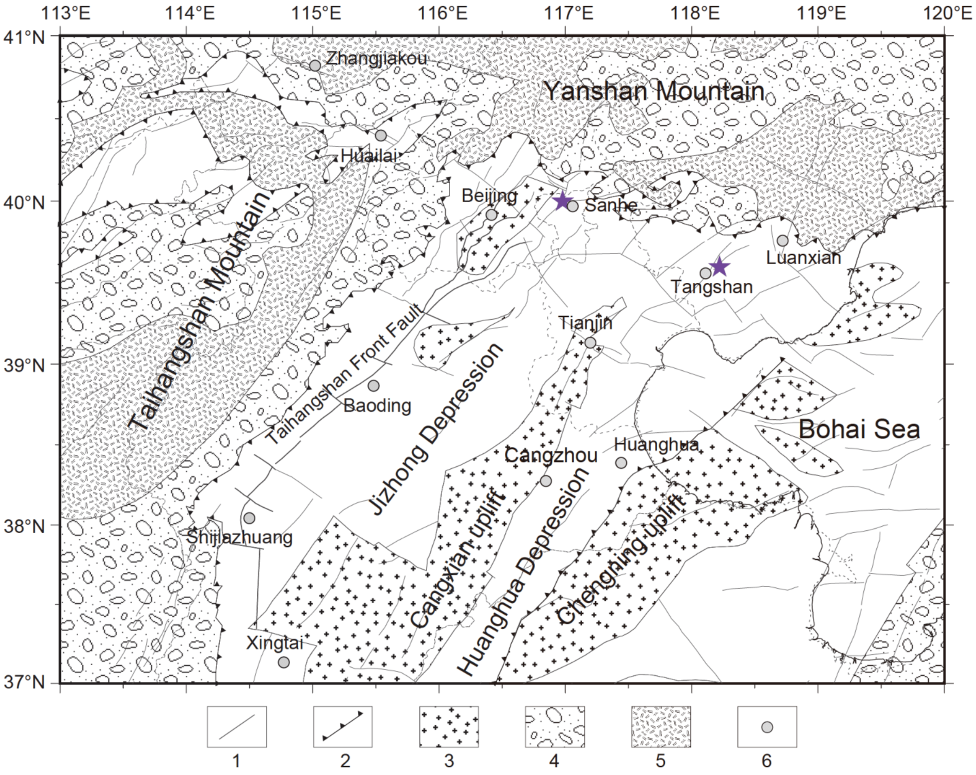

Figure 2 Tectonic map of the study area (after Huang and Zhao, 2004). The two stars represent the Sanhe-Pinggu earthquake and the Tangshan earthquake. The legend is shown at the bottom. 1, Major faults; 2, boundary of Cenozoic basins; 3, uplift areas in North China Basin; 4, granitic areas; 5, Pre-Cambrian basement; 6, cities.

Due to this complex tectonic background, studies concerning the fine crustal structures and dynamic mechanisms in the capital circle region, as well as the relationship between the complex structures and seismic activity, are of great significance.

Since the 1976 Tangshan earthquake, the subsurface structure of the capital circle region has been widely studied, with most of works focusing on the crust (i.e., Yu et al., 2003, 2010; Sun et al., 1993; Li et al., 2001; Huang and Zhao, 2004; Duan et al., 2016; Yang et al., 2018). Many works studied the upper mantle structures using teleseismic data (i.e., Jin et al., 1980; Shedlock and Roecker, 1987; Zhu et al., 1990; Huang and Zhao, 2009; Fu et al., 2015; Wang et al., 2017). The results of such studies show that there is a significant lateral difference in the P-wave velocity in the crust and upper mantle, with a relatively low-velocity anomalous zone existing in the southeast and high-velocity anomaly in the northwest (Jin et al., 1980). The difference is closely related to the seismicity at depth. Zhu et al. (1990) demonstrated that lateral heterogeneity is obvious in a depth range of 100 km in the Beijing-Tianjin-Tangshan-Zhangjiakou region and that the velocity anomalies are well correlated with the surface geology within a depth of 50 km. For example, the area beneath the Yanshan Uplift shows a high-velocity anomaly and the area under the depression zones show low-velocity anomalies, while most of the large earthquakes in the region occur in the transition zone between high-velocity and low-velocity anomalies (Lv, 2009). Zhang et al. (2007) indicated that the crustal velocities under the capital circle areas are affected by both the main tectonic units on the surface and deep fractures and that the velocity anomalies are distributed in an approximately NNE orientation arrangement, which can be characterized by belt in E-W direction but block in N-S direction. Lei et al. (2008) studied the 3-D P-wave velocity structure of the crust in the capital circle region by using both direct P-wave and the Moho reflection phase (PmP) simultaneously, which improved the seismic imaging resolution in the middle and lower crust. Studies on the anisotropy of the middle and upper crust in this region have shown a distinct structural feature in the intersection zone of the Taihangshan Uplift and the North China Basin (Gao et al., 2011). These studies provide significant evidence for us to understand dynamic mechanisms and the relationship between earthquake preparation and occurrence with the subsurface structures of the capital circle region.

The majority of these previous works are obtained by ray-based traveltime seismic tomography method, however, the distribution of stations is sparse and the traveltime data are not very accurate. Over the past decade, the China Earthquake Networks Center (CENC) has set up a number of high-precision broadband digital seismic stations in Beijing and its surrounding areas (Figure 3) and has accumulated abun-

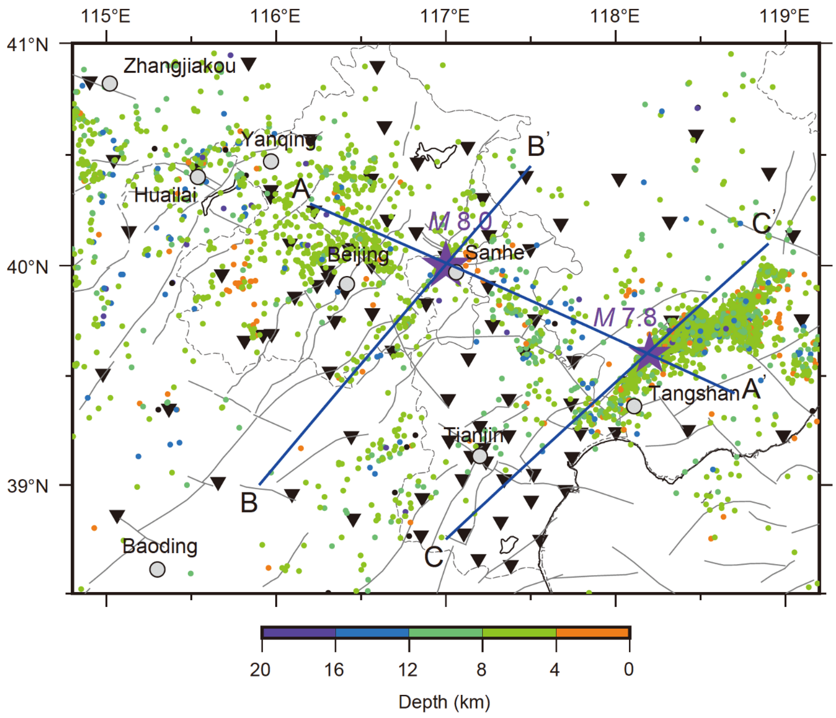

Figure 3 The distribution of the seismic stations and events used in this study. The dots represent the epicenters of event, with color representing the depth as the color-bar is shown at the bottom. The black inverse triangles are the station locations. The two purple stars represent the Sanhe-Pinggu earthquake and the Tangshan earthquake, respectively. The blue lines are the locations of three cross-sections.

dant high-precision seismic data. In this study, we use the quasi-waveform seismic tomographic method, which is based on numerically solving wave equations, to invert the 3-D P-wave, S-wave velocity and Poisson's ratio structures of the crust in the capital circle region. These models will help us obtain a new understanding of the fine velocity structures and the dynamic mechanisms of the crust, especially in the middle and upper crust, of the region.

2. The quasi-waveform seismic tomographic method

Waveform-based seismic tomography resolves the subsurface structures and deduces the media properties by establishing an objective function that directly minimizes the match between the observed and synthetic waveforms. The results of waveform-based seismic tomographic inversion are dependent on and sensitive to the initial model; therefore, an initial model that is consistent with the actual media is necessary (Liu and Gu, 2012; Virieux and Operto, 2009). An inaccurate initial model may lead to a distortion of the inverted results. As a precondition to the waveform-based inversion, a good initial model should satisfy the Born approximation in the waveform-based inversion method derivation. However, due to the complexity of geologic structures, it is difficult to accurately obtain synthetic waveforms that have a good match with the corresponding observed waveforms, especially high-frequency waveforms, by numerically solving wave equations in real applications. In addition, noise, which mixes with the observed waveform signals, and the periodic features of seismic waveforms make waveform matching even more difficult. Recently, Wang et al. (2019) developed a full waveform inversion method based on Kalman filtering and unreturned sampling, resulting in a larger convergence domain. This somewhat relieves the problem that the full waveform inversion method is initial model dependence, even though real application using observed waveform has not been realized and further studies need to be conducted. Challenges to using waveform-based seismic inversion methods in practice still exist, and valuable studies on numerically synthesizing accurate waveforms under the background of complex media models still have a long way to go. Currently, the traveltimes of certain phases are thought to be the most stable and reliable information that can be extracted from the observed data (Tong, 2012). Its validity has been confirmed by several studies using the traveltimes in actual seismic tomography inversions (Tong et al., 2014a, 2014b; Huang et al., 2016a; Tong et al., 2017; Dong et al., 2019). In this study, we develop a quasi-waveform seismic tomography method based on numerically solving the acoustic wave equations, in which the traveltimes of certain phases are used. Then, we use this method to conduct seismic tomographic inversions to achieve 3-D high resolution and reliable models of the crust in the capital circle region.

2.1 The quasi-waveform seismic tomographic method

The P- or S-wave traveling in isotropic media satisfies the acoustic wave equation:

$$\begin{cases} \dfrac{\partial^2 s(t,\mathbf{x})}{\partial t^2} = \nabla\cdot[c^2(\mathbf{x})\nabla s(t,\mathbf{x})] + f(t)\delta(\mathbf{x}-\mathbf{x}_s),\ \mathbf{x}\in\Omega; \\ s(0,\mathbf{x}) = \dfrac{\partial s(0,\mathbf{x})}{\partial t} = 0,\ \ \mathbf{x}\in\Omega; \\ \mathbf{n}\cdot[c^2(\mathbf{x})\nabla s(t,\mathbf{x})] = 0,\ \ \mathbf{x}\in\partial\Omega, \end{cases} \tag{1}$$

where $c(\mathbf{x})$ is either the P or S wave velocity model, $s(t, \mathbf{x})$ represents the pressure or the displacement field, f is the source time function for the point source at $\mathbf{x}_s$, and $\mathbf{n}$ is the normal direction of the boundary $\partial\Omega$. Suppose that $t_{\text{obs}}(\mathbf{x}_r, \mathbf{x}_s)$ and $t_{\text{syn}}(\mathbf{x}_r, \mathbf{x}_s)$ are respectively the observed traveltime and synthetic traveltime with initial model $c(\mathbf{x})$ of a certain seismic phase at the station $\mathbf{x}_r$ and define the misfit function of the observed and synthetic traveltimes as:

$$\chi(\mathbf{m},\mathbf{m}_0,\mathbf{x}_r) = t_{\text{obs}}(\mathbf{x}_r,\mathbf{x}_s) - t_{\text{syn}}(\mathbf{x}_r,\mathbf{x}_s), \tag{2}$$

where $\mathbf{m}$ is the real media model of the earth and $\mathbf{m}_0$ is a given initial model. For a perturbation $\delta\mathbf{m}$ of the initial model $\mathbf{m}_0$, a consequent perturbed traveltime $\Delta t(\mathbf{x}_r, \mathbf{x}_s)$ will be generated. Hereafter the eq. (2) can be rewritten as:

$$\begin{aligned}\chi(\mathbf{m},\mathbf{m}_0+\delta\mathbf{m},\mathbf{x}_r) = t_{\text{obs}}&(\mathbf{x}_r,\mathbf{x}_s) \\ &-t_{\text{syn}}(\mathbf{x}_r,\mathbf{x}_s) - \Delta t(\mathbf{x}_r,\mathbf{x}_s).\end{aligned} \tag{3}$$

Subtracting (3) from eq. (2), we can obtain

$$\begin{aligned}\delta\chi &= \chi(\mathbf{m},\mathbf{m}_0+\delta\mathbf{m},\mathbf{x}_r) - \chi(\mathbf{m},\mathbf{m}_0,\mathbf{x}_r) \\ &= -\Delta t(\mathbf{x}_r,\mathbf{x}_s).\end{aligned} \tag{4}$$

We can obtain the traveltime difference $\Delta t(\mathbf{x}_r, \mathbf{x}_s)$ using the cross-correlation function (Dahlen et al., 2000; Tong, 2012):

$$\begin{aligned}\delta\chi &= -\Delta t(\mathbf{x}_r,\mathbf{x}_s) \\ &= -\frac{\displaystyle\int_0^{\mathrm{T}} \omega(t)\delta s(t,\mathbf{x}_r)\frac{\partial s(t,\mathbf{x}_r)}{\partial t}\mathrm{d}t}{\displaystyle\int_0^{\mathrm{T}} \omega(t)s(t,\mathbf{x}_r)\frac{\partial^2 s(t,\mathbf{x}_r)}{\partial t^2}\mathrm{d}t}.\end{aligned} \tag{5}$$

Eq. (5) gives the relationship among the perturbed traveltime $\Delta t(\mathbf{x}_r, \mathbf{x}_s)$, the perturbed waveform $s(t, \mathbf{x}_r)$ and the waveform $s(t, \mathbf{x}_r)$. Therefore, the traveltime of a certain phase whether in the initial model or the perturbed model can be extracted from waveforms recorded by the stations. The equation in which $\delta s(t, \mathbf{x})$ is satisfied can be derived from the acoustic wave equations with models $\mathbf{m}_0$ and $\mathbf{m}_0+\delta\mathbf{m}$. Then the tomographic equation of the acoustic wave equation-based traveltime seismic tomography can be derived as follows using the adjoint method (Tromp et al., 2005), Green function method, one-order Born approximation and a series of mathematical derivations (Huang, 2016).

$$\begin{aligned}\Delta t(\mathbf{x}_r,\mathbf{x}_s) &= t_{\text{obs}}(\mathbf{x}_r,\mathbf{x}_s) - t_{\text{syn}}(\mathbf{x}_r,\mathbf{x}_s) \\ &= -\int_\Omega\left[\int_0^{\mathrm{T}} 2c_0^2(\mathbf{x})\nabla s^*(T-t,\mathbf{x})\cdot\nabla s(t,\mathbf{x})\,\mathrm{d}t\right] \\ &\quad\times\frac{\delta c(\mathbf{x})}{c(\mathbf{x})}\mathrm{d}\mathbf{x},\end{aligned} \tag{6}$$

where T is the duration of the waveform recording, and $s^*(t, \mathbf{x})$ is adjoint wave equation defined by the following equations (Tong et al., 2014a; Huang, 2016):

$$\begin{cases} \dfrac{\partial^2 s^*(t,\mathbf{x})}{\partial t^2} = \nabla\cdot[c^2(\mathbf{x})\nabla s^*(t,\mathbf{x})] \\ \qquad + \dfrac{\omega(T-t)\dfrac{\partial s(T-t,\mathbf{x})}{\partial t}\delta(\mathbf{x}-\mathbf{x}_r)}{\displaystyle\int_0^{\mathrm{T}}\omega(T-t)s(t,\mathbf{x}_r)\frac{\partial^2 s(t,\mathbf{x}_r)}{\partial t^2}\mathrm{d}t},\ \ \mathbf{x}\in\Omega; \\ s^*(T,\mathbf{x}) = \dfrac{\partial s^*(T,\mathbf{x})}{\partial t} = 0,\ \ \mathbf{x}\in\Omega; \\ \mathbf{n}\cdot[c^2(\mathbf{x})\nabla s^*(t,\mathbf{x})] = 0,\ \ \mathbf{x}\in\partial\Omega, \end{cases} \tag{7}$$

where $\omega(t)$ is a weight function over the time interval $[0,T]$ that can be used to isolate the certain seismic phases and $s(t, \mathbf{x}_r)$ is the waveform recorded at $\mathbf{x}_r$. Eq. (1) and the adjoint wave eq. (7) can be solved using the same numerical method since they are both acoustic wave equations and the only difference lies in the source term.

Eqs. (5) and (6) indicate that the traveltime extraction and the calculation of the tomographic equation rely on the waveform and the wavefield information, which is obtained by numerically solving the acoustic wave eqs. (1) and (7). Mathematically, eq. (6) can be expressed as a function of the original wavefield $s(\mathbf{x}_r, \mathbf{x}_s)$, which is relative to the source and station locations, and the adjoint wavefield $s^*(\mathbf{x}_r, \mathbf{x}_s)$ as follows

$$\Delta t(\mathbf{x}_r,\mathbf{x}_s) = F[s(\mathbf{x}_r,\mathbf{x}_s), s^*(\mathbf{x}_r,\mathbf{x}_s)]. \tag{8}$$

The tomographic method does not match the synthetic waveforms with the observed waveforms, nor does it calculate traveltimes by solving kinematic equations. However, it uses both the dynamic and kinematic information of the seismic waves, accordingly, we call it quasi-waveform seismic tomography.

2.2 Numerical method and model parameterization

The quasi-waveform seismic tomography method is based on numerically solving the forward wavefield (1) and the adjoint wavefield (7) to obtain waveforms at the receivers as well as the calculation of tomographic control eq. (6). If the gradient fields of forward wavefield and adjoint wavefield can be directly obtained when solving the acoustic wave equations, the accuracy is improved and therefore the results of the tomographic imaging are also improved either. As so far, several types of numerical algorithms have been developed for forward modeling in seismic tomography methods. For example, Chen et al. (2007) used the staggered-grid finite difference method as the forward operator to synthesize seismic waveforms and calculate sensitivity kernels. Tape et al. (2009, 2010) and Fichtner et al. (2010) used the spectral element method (SEM) to simulate the propagation of seismic waves in the earth's interior. Tong et al. (2014b) and Huang et al. (2016a, 2016b) used a finite difference method as the forward operator to solve the wave equations in seismic tomography. All of these methods have their merits and demerits, and their accuracy and computational efficiency directly affect the resolution of the inversion results and the validity of the inversion methods. In practice, tens of thousands or even millions of seismic records are generally used, which implies that a huge number of wave equations need be solved numerically. In this case, one of the keys to realizing a quasi-waveform seismic tomography method is to find an accurate and effective forward modeling tool. The nearly analytic discretization (NAD) method is such kind of finite difference method, that can directly obtain the gradient field as well as the wavefields simultaneously (Yang et al., 2003, 2004, 2006, 2012; Huang et al., 2016b). The method could improve the computational efficiency by suppressing numerical dispersion in a large grid scale, since the high-order partial derivatives in the difference method are approximated by both the displacement or the particle velocity and its gradients on grids to reconstruct an accurate wavefiled. Tong et al. (2014a) developed a simplified finite difference scheme based on the NAD method. It calculates the gradient fields by directly interpolating on the grid points, which allows for high computational efficiency, low memory requirements, high parallelism, and a straightforward acquisition of the gradients of the wavefield. In this study, we follow this high-order central difference scheme to solve the forward wavefields (1) and the adjoint wavefields (7).

In eq. (6), the ratio of the velocity perturbation to the true velocity $\delta c(\mathbf{x})/c(\mathbf{x})$ is calculated as the unknowns. Discretizing eq. (6) into a linear equation with M unknowns denoted by X, the equation can be rewritten as:

$$\sum_{i=1}^{M} a_i X_i = \Delta t(\mathbf{x}_r, \mathbf{x}_s), \tag{9}$$

where a_i is the coefficient of the i-th unknown. This linear equation represents the constraint on the space of the parameters to be inverted by the seismic record, which is generated at source $\mathbf{x}_s$ but recorded at station $\mathbf{x}_r$. The constraints supplied by all the used records form a linear algebraic equation system. Accordingly, the quasi-waveform inversion problem is converted into a linear algebraic equation system. When N seismic records are used to explore the subsurface structure, the N tomographic equations take the form of eq. (9) and form a linear system $AX=b$, where A is a matrix with size of $N\times M$ and is called the Fréchet matrix or the Jacobin matrix and b is the N-dimensional traveltime residual vector. Since the linear system is always ill-posed (either due to non-uniqueness or non-existence of X), a general way to solve it is to seek a solution that minimizes the following regularized objective function (Tong et al., 2014a):

$$\chi(X) = \frac{1}{2}(AX-b)^{\mathrm{T}}C_{\mathrm{d}}^{-1}(AX-b) + \frac{\varepsilon^2}{2}X^{\mathrm{T}}C_{\mathrm{m}}^{-1}X + \frac{\eta^2}{2}X^{\mathrm{T}}D^{\mathrm{T}}DX, \tag{10}$$

where C_{d} and C_{m} are the prior data and the model covariance matrix, respectively, and D is a derivative smoothing operator. The last two terms on the right-hand side of eq. (10) are regularization terms. ε and η are the damping and smoothing parameters, respectively, whose values control the balance among the degree of fitting of the solution and the data, the difference between the inversion model and the initial model, and the smoothness of the inverted model (e.g., Tarantola, 2005; Rawlinson et al., 2010; Tong et al., 2014a; Huang, 2016).

The implementation of the quasi-waveform seismic tomography method can be summarized as follows:

(1) Select the initial model $c_0(\mathbf{x})$, and set the stop criterion for iteration;

(2) Numerically solve the original wave eq. (1) and the adjoint wave eq. (7), to obtain $s(\mathbf{x}_r, \mathbf{x}_s)$ and $s^*(\mathbf{x}_r, \mathbf{x}_s)$;

(3) Discretize the control equation of the quasi-waveform seismic tomography (6) and obtain the linear algebraic equation system $AX=b$;

(4) Obtain the model update increment $\delta c(\mathbf{x})$ by solving the optimization problem (10) which is transformed from the linear system;

(5) Update the model $c(\mathbf{x})+\delta c(\mathbf{x})$;

(6) Stop iterating if the value of the objective function is less than the stop criterion set in (1), otherwise, turn to (2) for another iteration with the updated model $c(\mathbf{x})+\delta c(\mathbf{x})$ as the initial model.

3. Resolution tests

3.1 Data and initial model

In this study, we use the direct phases from January 2008 to May 2014 from the CENC, to invert for the crustal velocity structures of the capital circle region of China . The study area ranges from 114.8°E to 119.2°E in longitude, and 38.5°N to 41°N in latitude (as shown in Figure 1). All the events used in the inversion are local earthquakes and the source and station locations of the records are all within the study area. The events used in the inversion were strictly selected to reduce the influence of picking errors or nonuniform distribution.

The selection of the first arrivals was based on the following criteria (Huang, 2016). (1) Only events with more than 5 P and S arrivals were chosen. In general, the source is located with a reference model, and more first arrivals results in more accurate source locations. With this criterion we can reduce the dislocation of sources. (2) Seismic records with epicentral distances no more than 100 km were chosen. Seismic waves may reflect, scatter and diffract when traveling through the earth due to strongly heterogeneous of subsurface structures. The first arrival phase may mix with other phases, including reflected phases by deep interface, if the epicentral distance is greater than a certain range. In addition, the epicentral distance is directly related to the computational cost of the forward modeling and a large distance will bring challenges to the tomographic inversion. (3) The difference between the observed traveltime and the prediction time calculated for a 1-D reference model needs to be within 1.0 and 1.5 s for the P and S arrivals, respectively. Errors always exist when picking the traveltimes of phases. Mistakes in identifying phases may lead to large errors because there are many reflection phases that may mix with the first arrivals. A reasonable threshold can limit the error and ensure that the picked traveltime of the interested phase as accurate as the best. (4) The research area was divided into blocks with sizes of 5.0 km×5.0 km×1.0 km, and only one event with the maximum number of records is selected in each block to avoid the clustering of events. The constraints of the linear equations, which were obtained using a dense seismic event distribution, may have a strong correlation, resulting in the inverse problem being much more ill-posed. In this case many information is redundant. By limiting the number of seismic events within a block, the distribution of the seismic events tends to be uniform, which indirectly eases the ill-posed condition of the inversion problem (Qi et al., 2006). As a result, 29839 P first arrivals and 29972 S arrivals from 3231 local earthquakes were selected. The distribution of the selected events, which were recorded by 87 high-precision seismic stations in the study area, is shown in Figure 3. Overall, the stations cover the entire study area evenly, except for in the Bohai and other marginal regions.

Many studies have shown that internal discontinuities, such as the Conrad discontinuity and Moho discontinuity, have a significant effect on tomographic images, especially in areas with large lateral variations in the depth of the discontinuities (Zhu and Kanamori, 2000; Tian et al., 2007; Zhao et al., 2005; Huang et al., 2016a; Huang, 2016). Previous studies have shown that the depth of the Moho in North China varies strongly (Zhang, 1998; Li et al., 2001; Shi et al., 2014; Zhang et al., 2019). Therefore, in this paper, we used the depths of the Conrad and Moho discontinuities, as given by Zhang (1998) and Li et al. (2001), to constrain the tomographic imaging of the crustal velocity structures.

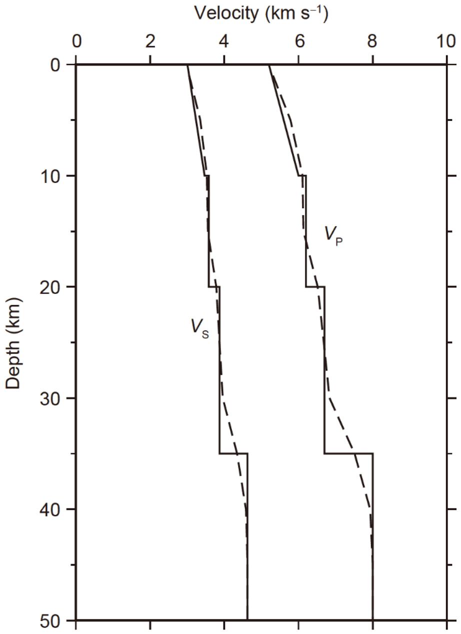

Figure 4 1-D velocity models, where the solid lines are the initial models and the dashed lines are the average inverted velocities at each depth.

We chose a 1-D layered model, which has been widely used in previous works (China Seismological Bureau, 1986; Huang and Zhao, 2004; Qi et al., 2006), as the initial velocity model as shown in Figure 4, where the two solid lines are the P- and S-wave velocity curves with depth, respectively. The apparent velocity discontinuities at 20 km and 35 km represent the Conrad and Moho discontinuities, respectively (Zhang, 1998; Li et al., 2001). In the forward modeling, the source time function is a Ricker wavelet with the following expression (Tong et al., 2014b):

$$f(t) = A\left[2\pi^2 f_0^2\left(t-\frac{1.2}{f_0}\right)^2-1\right] \times\exp\left[-\pi^2 f_0^2\left(t-\frac{1.2}{f_0}\right)^2\right], \tag{11}$$

where A is the amplitude, which we choose to be 1. f_0 is the dominant frequency. Considering both the magnitudes of the chosen events and the relationship between the corner frequency and the dominant frequency (Tong et al., 2011), we chose f_0 to be 2.0 Hz for the P-wave and 1.2 Hz for the S-wave with the magnitudes of events being limited from M1.0 to M4.0 (Huang, 2016).

Two different sets of grids were adopted in the tomographic inversion, one for forward modeling and another for inversion. The quasi-waveform seismic tomography method uses a '2D-3D' approximation method that projects the 2D forward grids into 3D inversion grids via interpolation; therefore, the forward grids can be determined in a 2-D vertical plane passing through the source and receiver (Tong et al., 2014b). A fine increment of approximately 0.2 km was used for the forward grids in this study to ensure the stability of the finite difference method and the accuracy of the numerical simulation. Inversion grids are set according to the resolution of the tomography method and the features of the seismic data used, such as the coverage of the events and stations, and therefore they are relatively coarse. In this study, the inversion grids were set as regular grids, as shown horizontally in Figure 5. The resolution was 0.15° in latitude and 0.2° in longitude in the central portion of the study area where the events and stations were dense, while it was 0.2° in latitude and 0.4° in longitude in the marginal areas. Vertically, the depths of the inversion grids were set to 1, 5, 10, 15, 20, 25, 30, 35, 40 and 45 km. There were typically 10 layers with intervals of 5 km covering the entire crust in the capital circle region (Huang, 2016).

3.2 Checkerboard tests

We conducted checkerboard resolution tests using the same data, initial model, and inversion grids before the tomographic imaging of the crustal structure in the capital circle region to test the resolution and reliability of the inverted results. The input checkerboard model with alternating positive and negative velocity perturbations of 5% was assigned to the 3-D inversion grid nodes, and the modeled the synthetic traveltimes were calculated by numerical simulations. The other parameters, including the forward and the inversion methods, were the same as those used for the actual seismic tomographic imaging. We concentrated on the inversion results within a depth of 25 km since these events were primarily located in the middle and upper crust (Figure 3).

Figures 6 and 7 show the inversion results of the checkerboard tests for P- and S-wave velocities, respectively, without additional iterations. As can be seen from the two figures, the checkerboard patterns in the middle and upper crust were well recovered. In particular, in the middle of the study area, not only was the positive and negative alternating velocity structure of the checkerboard model well recovered but the amplitudes of the anomalies were also basically resolved. The inverted results at 1 and 25 km were slightly worse than those at other depths, and the amplitudes of the anomalies in some regions were significantly different from the input model. The reason for the lower resolution near the surface may have resulted from the strongly correlated constraints due to the similar propagation directions of seismic waves that travel upward from depth. The lack of events and the poor coverage of the seismic data reduced the resolution of the inverted images at the depth of 25 km. Additionally, the smaller number of stations in southwest and southeast regions of the study area, the Bohai Bay area, and northeast of Hebei led to poor data coverage; consequently, the checkerboard structure is poorly resolved at a depth of 25 km. Traveltime picking errors generally exist in data processing, which may affect the resolution of the imaging results. For this reason, we additionally conducted checkerboard tests with random noise in the synthetic traveltimes, by adding random noise with a standard deviation of 0.1 s to the P-wave traveltimes and 0.173 s to the S-wave traveltimes. The results show that the input checkerboard model can still be well resolved even though the random noise in the traveltimes reduces the resolution of the tomographic images (see Figures S1 and S2 in Appendix, https://link.springer.com). In general, most of the studied region was well recovered in the checkerboard tests, excepting the areas with less data coverage due to the nonuniform station and event distributions and the use of only local seismic data. These tests indicate the importance of using high-quality data and uniform station and event distributions in seismic tomographic imaging. More dense station distributions or teleseismic data are required to further improve the resolution of the checkerboard tests. Accordingly, we focus on the inversion results in the middle portions of the study area where the checkerboard model was well recovered in the following tomographic imaging analysis.

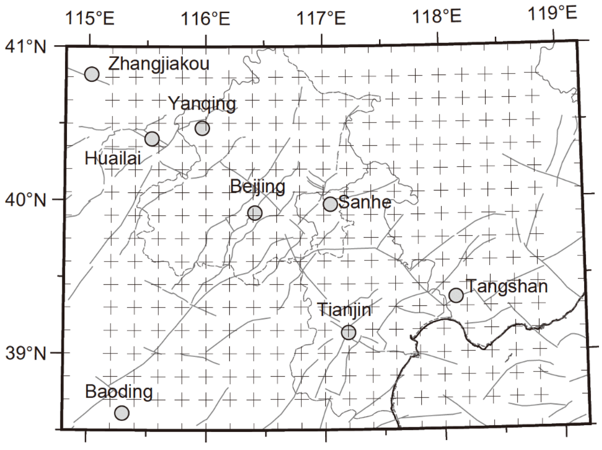

Figure 5 The inversion grid nodes, which is represented by the grey crosses. The grey curves are major faults.

4. Seismic tomography of the curst in capital circle region

The dashed lines in Figure 4 show the average velocity curves of the inverted velocity models, showing that the average velocities do not deviate much from the initial models and indicating the starting models are valid. We did not iterate the seismic tomography because, in addition to computational and time cost considerations, the results of the checkerboard tests have indicated that the anomalies were well resolved without additional iterations. The damping and smoothing parameters ε and η were given by the L-curve

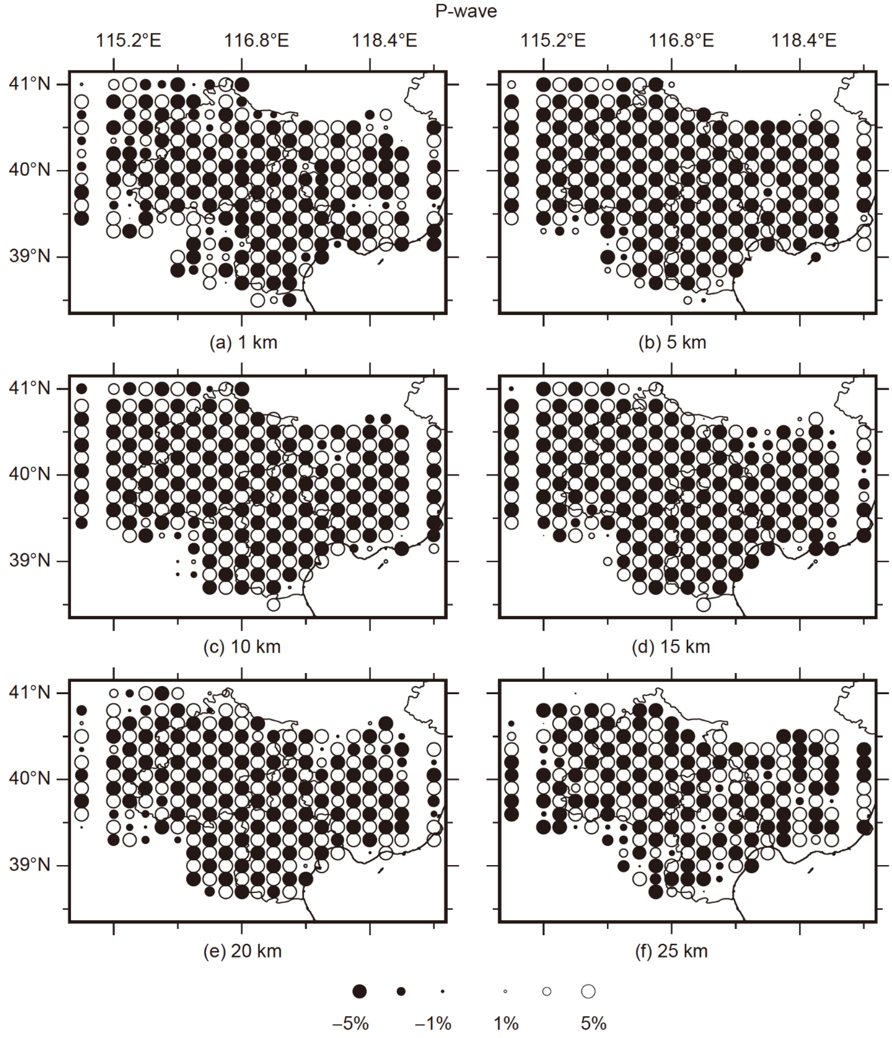

Figure 6 Inversion results obtained from the checkerboard test for P-wave velocity structures.

method (Tong et al., 2014b), where ε=2.5, and η=5.0 for P-wave velocity inversion, and ε=2.5, and η=5.5 for the S-wave velocity inversion. Figures 8 and 9 show the perturbations of the P- and S-wave velocities obtained using the quasi-waveform seismic tomography method with respect to the starting models. The inverted crustal models of the capital circle region illustrate the strong heterogeneity of the upper and middle crust (Huang and Zhao, 2004, 2009; Jia et al., 2005; Qi et al., 2006; Lv, 2009; Huang, 2016). At shallow depths (1–5 km), the distribution of the anomalies is generally correlated with the surface geology. In the southern Yanshan Uplift and the western Beijing, both the P- and S-wave velocities show relatively high anomalies due to the widely outcropping of the Paleozoic strata and Pre-Cambrian basement rocks on the surface (Qi et al., 2006; Huang and Zhao, 2004, 2009; Duan et al., 2016). Conversely, high-velocity anomalies in the uplift zones and low-velocity anomalies in the depression zones are alternatively distributed in the North China Basin. In particular, notable low-velocity anomalous belt zones are resolved between Beijing and Tianjin, and between Tangshan and Tianjin, corresponding to the Jizhong Depression and Huanghua Depression, respectively. The low-velocity anomaly in the Jizhong Depression is thicker than the others (Figures 8b and 9b). The Ninghe-Tangshan-Luanxian seismic belt is located inside the Huanghua Depression. Tianjin is located at a high-velocity anomaly corresponding to the Cangxian Uplift. The Taihangshan Front faults separate the Taihangshan Uplift, which shows a high-velocity anomaly, from the North China Basin, which shows low-velocity anomaly. Small intermontane basins, such as the Yanqing-Huailai Basin, which is located in the northwestern part of the study area, presenting a small range of low-velocity anomalies surrounded by high-velocity anomalies (Figures 8a and 9a) (Huang, 2016). The Taihangshan Mountain and Yanshan Mountain intersects there. The thicknesses of these low-velocity anomalies are generally less than 5 km, below which are mainly the granite and Pre-Cambrian basement rocks and showing high-velo-

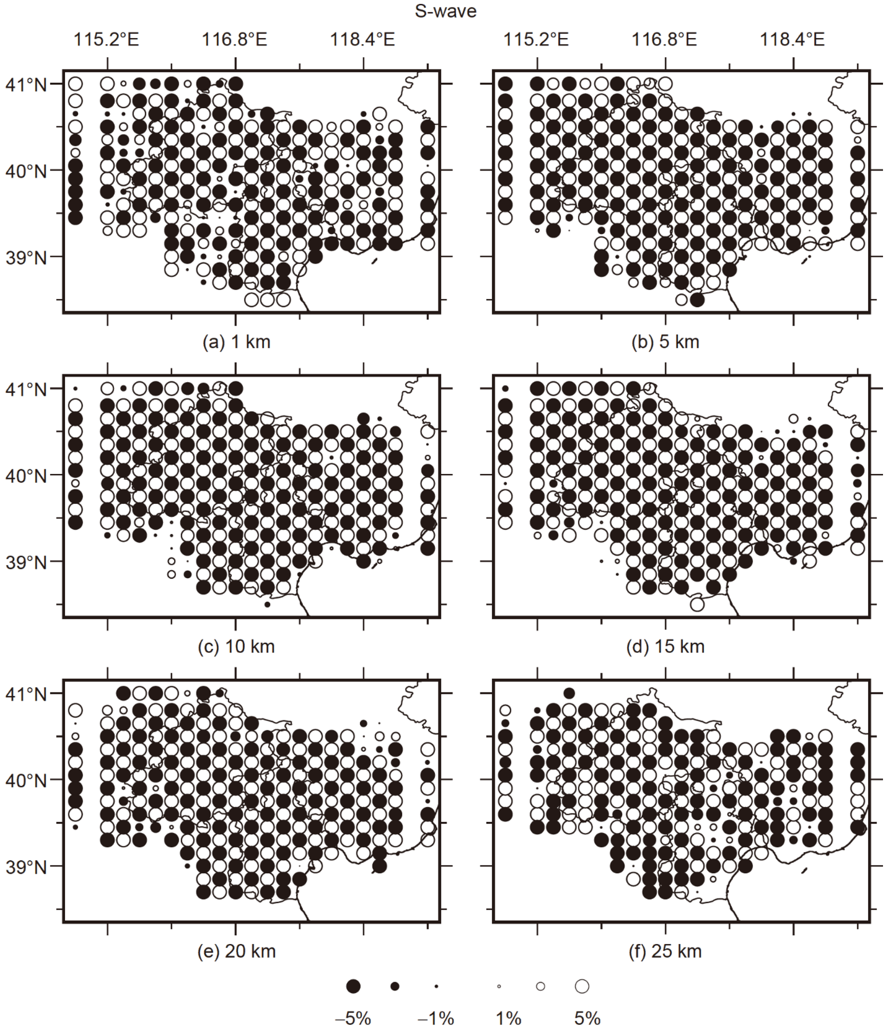

Figure 7 Inversion results obtained from the checkerboard test for S-wave velocity structures.

city anomalies. The low-velocity anomalies in intermontane basins may be due to sedimentation (Duan et al., 2016). In general, the heterogeneity at shallow depths shows an alternating pattern of high- and low-velocity anomalies with NE-SW orientation, which are separating from each other in the E-W direction and differing between the northern and southern portions. This is basically consistent with previous tomographic studies (Huang and Zhao, 2004, 2009; Jia et al., 2005; Qi et al., 2006; Lv, 2009; Duan et al., 2016).

High-velocity anomalies dominate at depths of 5 and 10 km (Figures 8b, 8c, 9b, 9c). However, low-velocity anomalies become the predominant feature at depths of 10–15 km. The velocities change rapidly in this depth range, which is considered as the dominant depth of seismicity (Zhao et al., 1993; Qi et al., 2006). The drastic change in the velocities may reflect interactions of strata with different properties, resulting in an unstable layer in the crust. The 1679 Sanhe-Pinggu earthquake (M8.0) had a focal depth of 13–15 km (Zhang et al., 2002), and the 1976 Tangshan earthquake had a focal depth of approximately 11 km. Both earthquakes were in the seismicity-prone depth range. Previous studies have shown that the occurrence of earthquakes often has a significant correlation with the transition zones between high- and low-velocity anomalies. Tomography studies in Japan by Zhao et al. (2002) show that large crustal earthquakes mainly occur on the boundaries between high- and low-velocity anomalies. Lin et al. (2007) demonstrated that the occurrence of earthquakes had a strong correlation with velocity anomalies in southern California. Tomographic studies in the capital circle region have similar conclusions (Jia et al., 2005; Qi et al., 2006; Huang and Zhao, 2004, 2009; Wang et al., 2017). The heterogeneity in the middle crust along the Ning-Tangshan-Luanxian is significant, and primarily shows low-velocity anomalies below the depth of 20 km. In addition, the low-velocity anomaly beneath Beijing at the same depth has a strong similarity to that beneath Tangshan. They are separated by a weak high-velocity anomaly with a NE-SW orientation. High-velocity anomalies

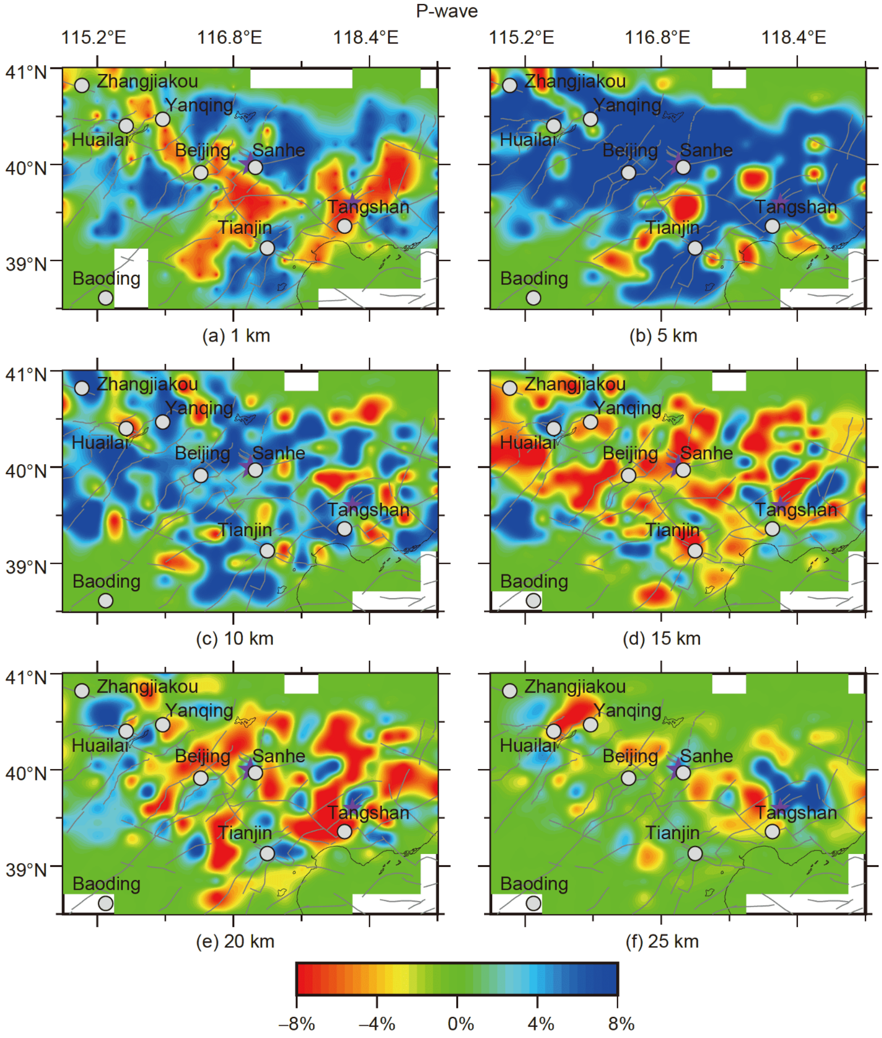

Figure 8 P-wave velocity perturbations at different depths. Blue and red colors represent high- and low-velocity perturbations, respectively, and the amplitudes of perturbations are given at the bottom. The two purple stars represent the Sanhe-Pinggu earthquake and the Tangshan earthquake, respectively. Major faults are represented by grey curves.

gradually appear with depth on the north of Tangshan.

Three typical vertical cross-sections (see Figure 3) were chosen to show the velocity variations with depth. The NW-SE profile AA′ crosses the epicenters of the Sanhe-Pinggu earthquake and the Tangshan earthquake, while the profiles BB′ and CC′ are roughly SW-NE passing through the two earthquakes respectively. The Poisson's ratio σ along the three profiles are also calculated based on the inverted P- and S-wave velocity models using the following formula (Tong et al., 2014a):

$$\left(\frac{V_\mathrm{P}}{V_\mathrm{S}}\right)^2=\frac{2(1-\sigma)}{1-2\sigma}. \tag{12}$$

Note that the differences in the resolution of P- and S-wave velocities caused by the data and the inversion parameters have an impact on the accurate of the Poisson's ratio. In the checkerboard tests, the input models along the three profiles were well resolved, showing that the inverted P- and S-wave velocities on these three profiles are relatively reliable and therefore discussing the Poisson's ratio anomalies qualitatively is meaningful.

Figure 10 shows the velocity perturbations of the P-wave (Figure 10a, 10d and 10g), S-wave (Figure 10b, 10e and 10h), and Poisson's ratio structures respect to the initial model (Figure 10c, 10f and 10i) along the three cross-sections. The velocities mainly have relatively high values near the surface (0–10 km) along the AA′ profile, except for a thin layer of low-value anomalies beneath the Beijing and Tangshan areas. The two cities are located in Jizhong and Huanghua Depressions and the thin low-velocity layer may infer to be the sedimentary caprocks. The velocities along AA′ profile are relatively high on shallow depths since this profile is located south of the Yanshan Uplift where there are Paleozoic strata and Pre-Cambrian bedrock at shallow depths (Huang and Zhao, 2004, 2009). The middle and lower crust are primarily relatively low-velocity anomalies, whose upper

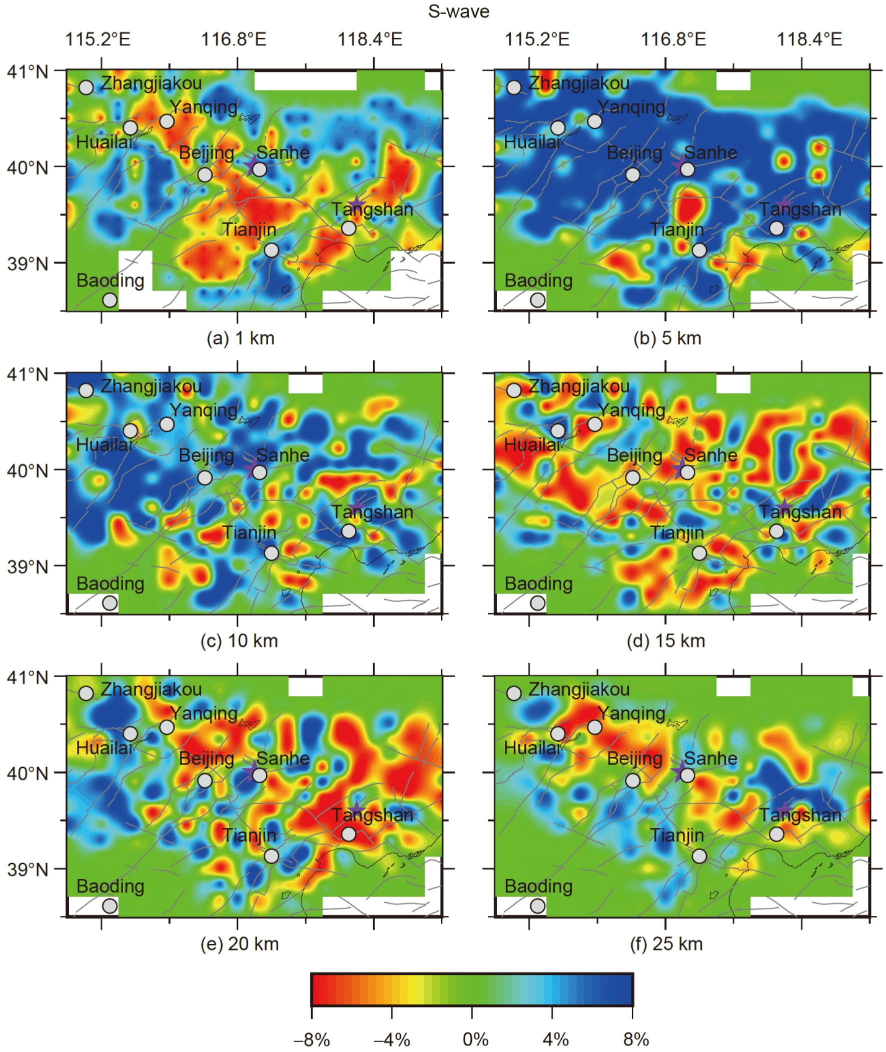

Figure 9 S-wave velocity perturbations at different depths. Symbols are the same as Figure 8.

boundaries are roughly consistent with the Conrad discontinuity. Duan et al. (2016) concluded that the presence of the low-velocity layer in the middle crust is an important geological characteristic in the central and eastern North China Craton, as the results of multiple phases of tectonic activity. There are obvious high-velocity anomalies below both the Sanhe-Pinggu earthquake (which is projected onto the profile at depth of 14 km) and the Tangshan earthquake. On the profile, both the P- and S-wave velocities show high degree of consistency near the sources of the two earthquakes. Above and below the sources, relatively high-velocity anomalies are presented with a thin low-velocity anomaly running between them. Both earthquakes occurred on the boundaries of high- and low-velocity anomalies, and the source of the Tangshan earthquake was on the side with high-velocity, which is consistent with earthquakes larger than *M*7.0 in Southwest China (Wang and Gao, 2014). However, we do not know whether the location of the Sanhe-Pinggu earthquake is the same as the Tangshan earthquakes, i.e., on the side with high-velocity or not, since the source depth is lack in historical data. In addition, several historical earthquakes larger than *M*5.0 along the profile occurred at the boundary of high- and low-velocity anomalies, and low Poisson's ratio anomalies, or transition zones between high and low Poisson's ratio anomalies, as found in previous works (Qi et al., 2006).

The BB′ profile is located in the Jizhong Depression, and its southern part shows a thin relatively low-velocity anomaly layer near the surface. The S-wave low-velocity anomaly is much significant. The north section of the profile is in the Yanshan Uplift area, showing high-V_P, and high-V_S anomalies with thicknesses of slightly more than 10 km. A relatively low-velocity anomaly is discovered below the high-velocity anomalies in the middle crust and is primarily distributed above the Conrad discontinuity. The low-velocity anomaly becomes weak and converts into weak V_S anomaly

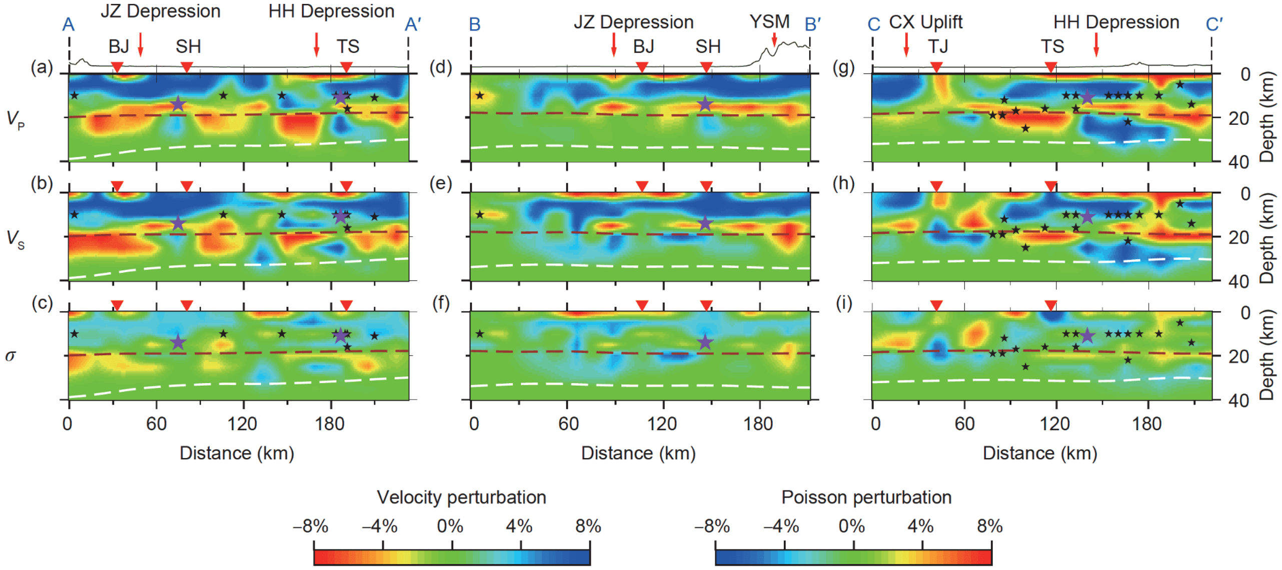

Figure 10 Vertical cross-sections of P-wave (V_P), S-wave (V_S) and the Poisson's ratio σ images along profile ((a)–(c)) AA′, ((d)–(f)) BB′ and ((g)–(i)) CC′ as indicated on the Figure 3 inset map. The white dashed curves represent the Moho discontinuity and the brown dashed curves represent the Conrad discontinuity. Red color denotes the low-velocity and high Poisson's ratio, while blue color shows high-velocity and low Poisson's ratio. Stars represent events with magnitudes greater than 5.0 in history, located within 10 km along the profiles. The two purple stars represent the Sanhe-Pinggu earthquake and the Tangshan earthquake, respectively. JZ, Jizhong; HH, Huanghua; BJ, Beijing; SH, Sanhe; TS, Tangshan; YSM, Yanshan Mountain; CX, Cangxian.

on the southwest of Beijing, but it becomes more obvious and thicker on the northeast as it extends into the Yanshan Uplift. The source of the Sanhe-Pinggu earthquake projected on this profile is on the boundary of high- and low-velocity anomalies and a low Poisson's ratio region either. From the perspective of geologic structure, the Sanhe-Pinggu earthquake located in the transition zone between the Yanshan Uplift and the subsidence area of the North China Plain. Two faults with NNE and near E-W directions meet there, forming a complex geological region (Zhang et al., 2002). Sanhe divides the BB′ profile into northern and southern sections. The vertical structures are consistent of the two section, where there are thin low-velocity anomalies near the surface, high-velocity anomalies dominating in the upper crust, and a low-velocity anomaly in the middle crust. The Poisson's ratio has a similar structure but weaker amplitudes than the velocity perturbations. These results are similar to the reflection wave detection results obtained by Zhang et al. (2002).

The CC′ profile extends NE-SW along the Ninghe-Tangshan-Luanxian earthquake belt and is primarily in the Huanghua Depression. Two large aftershocks of the 1976 Tangshan earthquake, the Luanxian earthquake (*M*7.1), which was located 25 km NE, and the Ninghe earthquake (*M*6.9), which was located 20 km SW, are on the profile with focal depths of 8 and 17 km, respectively. The southern portion of the profile extends into the Cangxian Uplift area, showing strong high-velocity anomalies in the upper part but weak low-V_P, strong low-V_S and high Poisson's ration anomalies in the lower part. The profile is in the Huanghua Depression on the north of Tianjin, showing a relatively low-velocity layer with a thickness of less than 5 km near the surface (Figure 10g–10h). The low-velocity anomaly below Tianjin separates the Cangxian Uplift and Huanghua Depression, and connects to the low-velocity layer at the depth of Conrad discontinuity. On northeast Tianjin, there is a high-velocity anomaly layer with a thickness of approximately 10 km between the low-velocity anomalies at shallow depths and the Conrad discontinuity. Several earthquakes with magnitudes larger than 5.0 along this profile are located on the bottom of the high-velocity anomaly but top of the low-velocity anomaly in the middle crust (Figure 10g–10h). The low P-wave anomaly presented at the bottom of the high-velocity anomaly is deeper than that on the north of the Tangshan earthquake and extends through the Conrad discontinuity to the lower crust. The S-wave is similar but low-velocity anomaly has a smaller size. The earthquakes in this section are distributed around the edge of the S-wave low-velocity anomaly. North of the Tangshan earthquake, the low-velocity anomaly tends to thicken gradually but has an obvious high-velocity anomaly beneath it. The Poisson's ratio along this profile is slightly more complicated than that of the AA′ and BB′ profiles, and earthquakes along this profile primarily locate in the low Poisson's ratio side of the boundary of high and low Poisson's ratio anomalies. In general, a strong heterogeneity pattern in the vertical is revealed in this profile and the number of layers increases from south to north. One important cause of the seismicity activity in this region may due to the strong crustal heterogeneity.

5. Discussion and conclusions

In this paper, we used the direct phases offered by CENC from January 2008 to May 2014, to invert for the crustal velocity structures of the capital circle region of China. 3-D high-resolution P- and S-wave velocity and Poisson's ratio models were obtained. Checkerboard tests demonstrated the resolution and reliability of the method. For the first time using the quasi-waveform seismic tomography method in crustal structure imaging, we obtained inversion results either using the ray-based traveltime tomography method (Tong et al., 2017) with the same data and inversion parameters to confirm the validity of the new method and compare the resolution of the two methods. Figure 11 shows a comparison of the velocity perturbation distributions of the P- and S-waves obtained along the AA′ and CC′ profiles. In general, the results obtained by the two methods are similar. For example, the upper crust is dominated by high-velocity anomalies and obvious low-velocity anomalies can be seen beneath this high-velocity layer. Historical earthquakes with magnitudes of 5.0 or larger mainly occurred on the boundaries of high- and low-velocity anomalies along the two profiles. Especially for the Sanhe-Pinggu earthquake and Tangshan earthquake, there are obvious relatively low-velocity anomalies below the sources. Along the CC′ profile, high-velocity anomalies in the upper crust on the south of Tianjin correspond to the Cangxian Uplift and the structures on the north of Tangshan revealed by the two methods both show complex patterns but obvious layered structures. However, in addition to these common features, the results of the quasi-waveform seismic tomography show some more detailed structures. For example, thin relatively low-velocity anomalies can be seen near the surface below Tangshan and Beijing, corresponding to the two geologic units, Jizhong Depression and Huanghua Depression, respectively. The low-velocity anomaly near the Conrad discontinuity shows a complex pattern. Small high-velocity anomalies exist below the low-velocity anomalies which are beneath the hypocenters of the Sanhe-Pinggu earthquake and the Tangshan earthquake . The high-velocity anomaly under the low-velocity region below the Tangshan earthquake is obvious along the CC′ profile, while the results obtained by the ray-based method only show a large range of low velocities. The results of the checkerboard tests imply that the inverted structures within the depth of 25 km are reliable; however, low velocities still can be seen below the Moho discontinuity in the results given by the ray-based method. This is likely artifacts due to the lack of data at the depths. Note that the quasi-waveform seismic tomography method still faces computational and storage cost challenges due to that a large number of wave equations need to be solved to obatin the synthetic traveltimes and the linear algebraic system during the inversion. Meanwhile, the ray-based method can be completed in a short time by a desktop computer, even though the quasi-waveform method shows a better performance in terms of its resolution and the anomalies revealed match the surface geologic structures much better. However, with the development of high-performance computers and computing technologies, the limitation of computational resources on the quasi-waveform method will become increasingly smaller.

The inverted crustal models of the capital circle region obtained by the quasi-waveform inversion reveal the strong heterogeneity of the crust. At shallow depths, the velocity anomaly structures are closely related to the surface topography and geologic structures. In the Yanshan Uplift and the Taihangshan Uplift, which are in the northern and western portions of the study area, the velocities are generally relatively high due to the widely outcropping of the Paleozoic strata and Pre-Cambrian basement rocks on the surface (Huang, 2016). The geologic units in the North China Basin, which are all roughly with NE-SW orientation, correspond well to the inverted velocity structures. The Jizhong Depression and the Huanghua Depression primarily correspond to low-velocity anomalies while the Cangxian Uplift corresponds to high-velocity anomalies. The Taihangshan Front fault zone is an intermediate separation zone that separates the high-velocity zone of the Taihangshan Uplift from the low-velocity zone corresponding to the Jizhong Depression in the North China Basin (Huang, 2016). The heterogeneity is more significant in the vertical direction along the Ninghe-Tangshan-Luanxian seismic belt. Generally speaking, earthquakes in the capital circle primarily occured on the boundaries of high- and low-velocity and Poisson's ratio anomalies. The widely discovered low-velocity layer in the middle crust is consistent with the conclusion of Duan et al. (2016). This low-velocity layer, which is nearly at the same depth as the Conrad discontinuity in the middle crust, exists intermittently in the E-W direction but continuously in the NE-SW direction. This feature is consistent with the distribution trend of the main geologic structures, and its formation may be due to subsidence, cracks, or other tectonic activities in North China and its surrounding areas in the tertiary and quaternary periods (Lv, 2009; Huang, 2016; Wang et al., 2017).

The crustal structures under Tangshan and Beijing revealed by this study have obvious similarities. A weak NE-SW orientation high-velocity anomaly belt separates the two regions in the middle crust. The similarities in their subsurface velocity structures may indicate that there is a correlation between the earthquakes occurrence in these two regions. The *M*8.0 Sanhe-Pinggu earthquake, which occurred east of Beijing in 1679, and the *M*7.8 Tangshan earthquake, which occurred in Tangshan in 1976, are representative earthquakes in the two regions. The relationship between the detailed mechanisms, the causes of the two

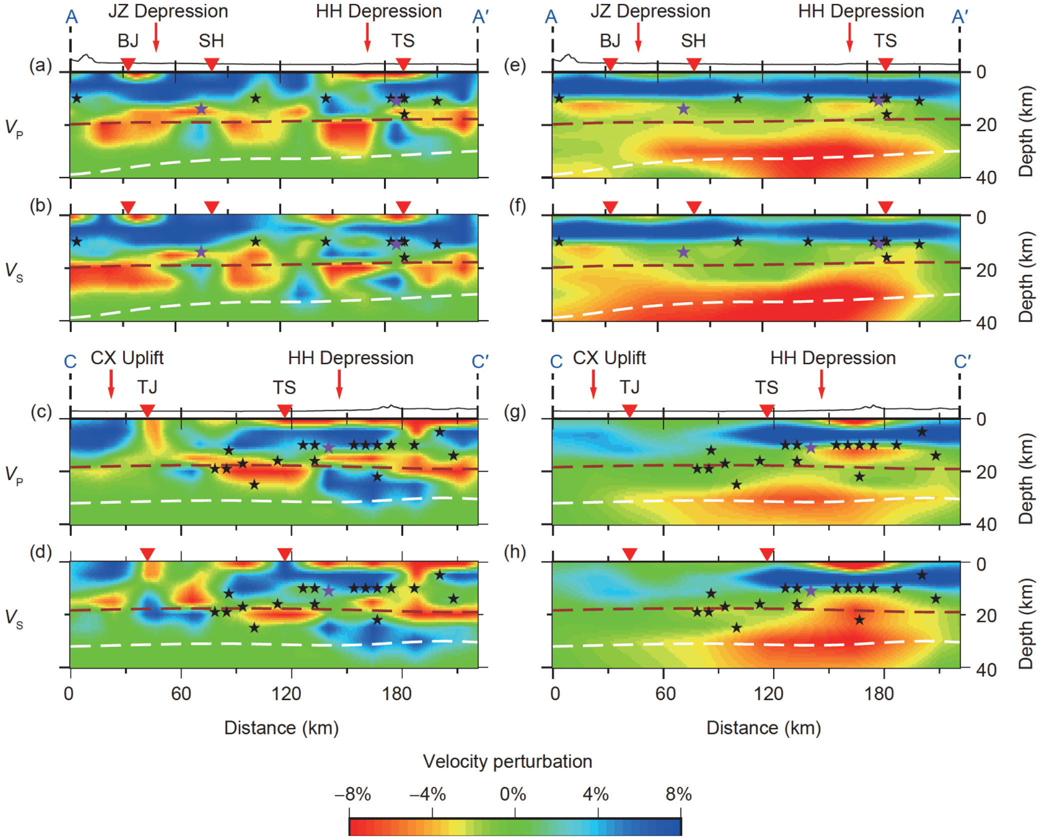

Figure 11 Comparison of the inversion results obtained by the Quasi-waveform method and the ray-based method along the cross-sections AA′and CC′. The left column subfigures ((a)–(d)) are the results obtained the quasi-waveform method, and the right column subfigures ((e)–(h)) are the results obtained the ray-based method.

earthquakes and the similarities in the subsurface structures of the two regions is one of the focuses of regional seismology and geodynamic studies.

Previous studies on the relationship between the crustal structure and the occurrence of strong earthquakes in the Beijing-Tianjin-Tangshan area had shown that the Tangshan earthquake and the Sanhe-Pinggu earthquake were located in very similar tectonic backgrounds and occurred in rapidly velocities changing positions (Yu et al., 2010; Sun et al., 1993; Zhang et al., 2002), which was consistent with our results. Similar conclusions had been obtained in studies of source areas of strong earthquakes in other regions. Tong et al. (2011) studied the source area of the 1995 Kobe earthquake in Japan and found that the earthquake occurred on the boundary of high- and low-velocity anomalies and that there was an obvious low-velocity anomaly under its hypocenter. Zhao et al. (2002) revealed that strong crustal earthquakes in Japan occurred on the boundaries of high- and low-velocity anomalies and that low-velocity anomalies beneath sources of these earthquakes in the crust is a common feature, and they inferred that as being related to the underplating of upwelling materials due to plate dehydration and magmatic activities. Wang and Gao (2014) revealed that earthquakes greater than *M*7.0 in the southeastern front area of the Tibetan Plateau generally occurred around the transition zones of high- and low-velocity anomalies but on the high-velocity side. Previous studies have indicated that the low-velocity anomalies below the sources may be one of the main causes of the Tangshan earthquake and its two larger aftershocks (Huang and Zhao, 2005; Qi et al., 2006). They concluded that these low-velocity bodies were characterized by high conductivity, high-heat flow value and negative gravity anomaly, implying high-temperature anomalies and the existence of fluids, resulting in the seismogenic layer in the middle and upper crust being weaken. Thereafter strong earthquakes were induced by the stress concentrating in these weak parts of the crust. However, Xu (2003) concluded that the Tangshan earthquake and most of its aftershocks occurred above the high conductivity layer and the source areas were with low calorific value. The earthquake sequence could not be attributed to the high temperature anomaly, and thereby inferring the earthquakes were primarily caused by the migration of deep fluids (Nakajima et al., 2001). The reason for the frequent occurrence of small and medium earthquakes in this area can also be attributed to the transfer and diffusion of fluids in the low-velocity anomalies (Qi et al., 2006). Sun et al. (1993) believed that the two large aftershocks and the mainshock of the Tangshan earthquake had different focal mechanisms. The North China Basin, the Bozhong Depression and the lower Xia-Liaohe Depression had different influences on the Tangshan earthquake sequence. However, as large aftershocks of the Tangshan earthquake, erosion and the weakening effect of fluid on the rocks may also have been important reasons for the Ninghe and Luanxian earthquakes, excepting the stress change and the migration and destruction of the rock strata caused by the mainshock of the Tangshan earthquake (Huang, 2016).

Zhang et al. (2002) studied the source area of the Sanhe-Pinggu earthquake and revealed that the velocity structure of the Sanhe-Pinggu area is laterally different significantly from the adjacent area. The Sanhe-Pinggu area is located in the transition zone of high- and low-velocities and has strong heterogeneity in both the horizontal and vertical directions. Our results confirm the conclusion, and the small high-velocity patches revealed in this paper may correspond to the local strong reflection energy group discovered below the hypocenter of the Sanhe-Pinggu earthquake. Zhang et al. (2002) inferred that there exist dykes or rock masses formed by the upwelling and subsequent cooling of upper mantle material. Differences in the local stress distribution due to magmatic activity may have resulted in deep faults in the crust, leading to the M8.0 Sanhe-Pinggu earthquake. This process is similar to that associated with the occurrence of the Tangshan earthquake, which is thought to be the result of fluid erosion and magmatic activity. The results of the quasi-waveform inversion reveal the high similarity of the source areas of these two large earthquakes, providing new evidence for these conclusions.

Regardless of how the Sanhe-Pinggu earthquake, the Tangshan earthquake and their aftershocks occurred, the fact that all of their hypocenters are in transition zones between high- and low-velocity anomalies is sufficient to conclude that the crustal heterogeneity in the capital circle region is an important factor affecting the occurrence of these earthquakes. The occurrence of large earthquakes is not only a simple mechanical question, but also closely related to the physical and chemical properties of the crust (Qi et al., 2006; Zhao et al., 2002; Huang, 2016). The detailed regional anomaly structures discovered by high-resolution seismic tomographic study provide important evidence to understand the preparation and occurrences of earthquakes. However, the relationships between the discovered anomaly structures, the physical and chemical properties of the media and the occurrences of large earthquakes need to be studied further.

Acknowledgements *The authors thank the anonymous reviewers for their valuable comments. Seismic data used in this study are from the CENC. This study was supported by the National Natural Science Foundation of China (Grant Nos. U1839206, 41230210). Huang X. was supported by the National Natural Science Foundation of China (Grant No. 41704047). Wu H. was also supported by the National Natural Science Foundation of China (Grant No. 11871297) and Tsinghua University Initiative Scientific Research Program. All figures are made with the Generic Mapping Tool (GMT).*

References

Chen P, Zhao L, Jordan T H. 2007. Full 3D tomography for the crustal structure of the Los Angeles region. Bull Seismol Soc Am, 97: 1094–1120

China Seismological Bureau E. 1986. Results of Crustal and Upper Mantle by Deep Geophysical Prospecting in China (in Chinese). Beijing: Seismological Press

Dahlen F A, Hung S H, Nolet G. 2000. Fréchet kernels for finite-frequency traveltimes—I. Theory. Geophys J Int, 141: 157–174

Dong X P, Yang D H, Niu F L. 2019. Passive adjoint tomography of the crustal and upper mantle beneath eastern Tibet with a W2-norm misfit function. Geophys Res Lett, 46: 12986–12995

Duan Y H, Wang F Y, Zhang X K, Lin J Y, Liu Z, Liu B F, Yang Z X, Guo W B, Wei Y H. 2016. Three-dimensional crustal velocity structure model of the middle-eastern North China Craton (HBCrust1.0). Sci China Earth Sci, 59: 1477–1488

Fichtner A, Kennett B L N, Igel H, Bunge H P. 2010. Full waveform tomography for radially anisotropic structure: New insights into present and past states of the Australasian upper mantle. Earth Planet Sci Lett, 290: 270–280

Fu Y V, Gao Y, Li A, Shi Y. 2015. Lithospheric shear wave velocity and radial anisotropy beneath the northern part of North China from surface wave dispersion analysis. Geochem Geophys Geosyst, 16: 2619–2636

Gao Y, Wu J, Fukao Y, Shi Y, Zhu A. 2011. Shear wave splitting in the crust in North China: Stress, faults and tectonic implications. Geophys J Int, 187: 642–654

Huang J, Zhao D. 2004. Crustal heterogeneity and seismotectonics of the region around Beijing, China. Tectonophysics, 385: 159–180

Huang J, Zhao D. 2009. Seismic imaging of the crust and upper mantle under Beijing and surrounding regions. Phys Earth Planet Inter, 173: 330–348

Huang J L, Zhao D P. 2005. Three-dimension P-wave velocity structure of the crust beneath the capital circle and the deep tectonic environment of strong earthquake (in Chinese). Chin Sci Bull, 50: 348–355

Huang X, Yang D, Tong P, Badal J, Liu Q. 2016a. Wave equation-based reflection tomography of the 1992 Landers earthquake area. Geophys Res Lett, 43: 1884–1892

Huang X, Yang D, Tong P, Zhou Y. 2016b. 3D nearly analytic central difference method for computation of sensitivity kernels of wave-equation-based seismic tomography. Bull Seismol Soc Am, 106: 2877–2899

Huang X Y. 2016. Wave equation-based seismic tomography method and their applications. Doctoral Dissertation. Beijing: Tinghua University

Jia S X, Qi C, Wang F Y, Chen Q F, Zhang X K, Chen Y. 2005. Three-dimensional crustal gridded structure of the Capital area (in Chinese). Chin J Geophys, 48: 1316–1324

Jin A S, Liu F T, Sun Y Z. 1980.Three-Dimensional P Velocity Structure of the Crust and upper Mantle under Beijing Region (in Chinese). Chin J Geophys, 23: 172–182

Lei J, Xie F, Lan C, Xing C, Ma S. 2008. Seismic images under the Beijing region inferred from P and PmP data. Phys Earth Planet Inter, 168: 134–146

Li S L, Zhang X K, Song Z L, Shi J H, Deng H Z, Yang J, Zhang C K, Ren Q F. 2001. Three-dimensional crustal structure of the capital area obtained by a joint inversion of deep seismic sounding data from multiple profiles. Chin J Geophys, 44: 357–365

Lin G, Shearer P M, Hauksson E, Thurber C H. 2007. A three-dimensional crustal seismic velocity model for southern California from a composite event method. J Geophys Res, 112: B11306

Liu G. 1987. The Cenozoic rift system of the North China Plain and the deep internal process. Tectonophysics, 133: 277–285

Liu Q, Gu Y J. 2012. Seismic imaging: From classical to adjoint tomography. Tectonophysics, 566-567: 31–66

Lv Z Y. 2009. Seismic tomography beneath the North China. Dissertation for Master's Degree. Beijing: Institute of Geophysics, China Earthquake Administration

Ma W T, Xu X W, Yu G H, Zhang L F. 2004. The relationship between the seismicity and the faults in Capital circle (in Chinese). Seismol Geol, 26: 293–304

Nakajima J, Matsuzawa T, Hasegawa A, Zhao D. 2001. Three-dimensional structure of V_P, V_S, and V_P/V_S beneath northeastern Japan: Implications for arc magmatism and fluids. J Geophys Res, 106: 21843–21857

Qi C, Zhao D P, Chen Y, Chen Q F, Wang B S. 2006. 3-D P and S wave velocity structures and their relationship to strong earthquakes in the Chinese capital region (in Chinese). Chin J Geophys, 49: 805–815

Rawlinson N, Pozgay S, Fishwick S. 2010. Seismic tomography: A window into deep Earth. Phys Earth Planet Inter, 178: 101–135

Shedlock K M, Roecker S W. 1987. Elastic wave velocity structure of the crust and upper mantle beneath the North China Basin. J Geophys Res, 92: 9327–9350

Shi Y T, Gao Y, Jing H L. 2014. Crustal thickness and V_P/V_S ratio in Shanxi Graben, China. Earthq Sci, 27: 589–597

Sun R, Zhao Y, Mei S. 1993. Seismic tomography image in Bohai Sea and adjacent area (in Chinese). Chin J Geophys, 36: 44–54

Tape C, Liu Q, Maggi A, Tromp J. 2009. Adjoint tomography of the southern California crust. Science, 325: 988–992

Tape C, Liu Q, Maggi A, Tromp J. 2010. Seismic tomography of the southern California crust based on spectral-element and adjoint methods. Geophys J Int, 180: 433–462

Tarantola A. 2005. Inverse problem theory and methods for model parameter estimation. SIAM, doi: 10.1137/1.9780898717921

Tian Y, Zhao D, Sun R, Teng J. 2009. Seismic imaging of the crust and upper mantle beneath the North China Craton. Phys Earth Planet Inter, 172: 169–182

Tian Y, Zhao D, Teng J. 2007. Deep structure of southern California. Phys Earth Planet Inter, 165: 93–113

Tong P, Zhao D, Yang D. 2011. Tomography of the 1995 Kobe earthquake area: Comparison of finite-frequency and ray approaches. Geophys J Int, 187: 278–302

Tong P. 2012. Seismic tomography method and their applications. Dissertation for Doctoral Degree. Beijing: Tsinghua University

Tong P, Zhao D, Yang D, Yang X, Chen J, Liu Q. 2014a. Wave-equation-based travel-time seismic tomography—Part 1: Method. Solid Earth, 5: 1151–1168

Tong P, Zhao D, Yang D, Yang X, Chen J, Liu Q. 2014b. Wave-equation-based travel-time seismic tomography—Part 2: Application to the 1992 Landers earthquake (M_w7.3) area. Solid Earth, 5: 1169–1188

Tong P, Yang D, Li D, Liu Q. 2017. Time-evolving seismic tomography: The method and its application to the 1989 Loma Prieta and 2014 South Napa earthquake area, California. Geophys Res Lett, 44: 3165–3175

Tromp J, Tape C, Liu Q. 2005. Seismic tomography, adjoint methods, time reversal and banana-doughnut kernels. Geophys J Int, 160: 195–216

Virieux J, Operto S. 2009. An overview of full-waveform inversion in exploration geophysics. Geophysics, 74: WCC1–WCC26

Wang C Y, Wu Q J, Duan Y H, Wang Z S, Lou H. 2017. Crustal and upper mantle structure and deep tectonic genesis of large earthquakes in North China. Sci China Earth Sci, 60: 821–857

Wang J, Yang D, Jing H, Wu H. 2019. Full waveform inversion based on the ensemble Kalman filter method using uniform sampling without replacement. Sci Bull, 64: 321–330

Wang Q, Gao Y. 2014. Rayleigh wave phase velocity tomography and strong earthquake activity on the southeastern front of the Tibetan Plateau. Sci China Earth Sci, 57: 2532–2542

Xu C F. 2003. Study on the cause of high conductive layer of the crust and upper mantle in Chinese mainland and the mechanism of Tangshan earthquake (in Chinese). Earth Sci Front, 10(Suppl): 101–111

Yang D. 2006. Optimal nearly analytic discrete approximation to the scalar wave equation. Bull Seismol Soc Am, 96: 1114–1130

Yang D, Lu M, Wu R, Peng J. 2004. An optimal nearly analytic discrete method for 2D acoustic and elastic wave equations. Bull Seismol Soc Am, 94: 1982–1992

Yang D, Peng J, Lu M, Terlaky T. 2003. A nearly analytic discrete method for acoustic and elastic wave equations in anisotropic media. Bull Seismol Soc Am, 93: 882–890

Yang D, Tong P, Deng X. 2012. A central difference method with low numerical dispersion for solving the scalar wave equation. Geophys Prospect, 60: 885–905

Yang Y, Yao H, Zhang P, Chen L. 2018. Crustal azimuthal anisotropy in the trans-North China orogen and adjacent regions from receiver functions. Sci China Earth Sci, 61: 903–913

Ye H, Shedlock K M, Hellinger S J, Sclater J G. 1985. The North China Basin: An example of a Cenozoic rifted intraplate basin. Tectonics, 4: 153–169

Ye H, Zhang B, Mao F. 1987. The Cenozoic tectonic evolution of the Great North China: Two types of rifting and crustal necking in the Great North China and their tectonic implications. Tectonophysics, 133: 217–227

Yu X W, Chen Y T, Zhang H. 2010. Three-dimensional crustal P-wave velocity structure and seismicity analysis in Beijing-Tianjin-Tangshan Region (in Chinese). Chin J Geophys, 53: 1817–1828

Yu X W, Chen Y T, Wang P D. 2003. 3-D P wave velocity structure of upper-mid crust in Beijing-Tianjin-Tangshan region (in Chinese). Acta Seismol Sin, 25: 1–14

Zhang L, Liu J S, Hao T Y, Liu J H, Xu Y. 2007. Seismic tomography of the crust and upper mantle in the Bohai Bay Basin and its adjacent regions. Sci China Ser D-Earth Sci, 50: 1810–1822

Zhang P, Yao H, Chen L, Fang L, Wu Y, Feng J. 2019. Moho depth variations from receiver function imaging in the Northeastern North China craton and its tectonic implications. J Geophys Res-Solid Earth, 124: 1852–1870

Zhang X K, Zhao J R, Liu G H, Song W R, Liu B J, Zhao C B, Cheng S X, Liu J D, Gu M L, Sun Z G. 2002. Study on fine crustal structure of the Sanhe- Pinggu Earthquake (M8.0) Region by deep seismic reflection profiling (in Chinese). Earthq Res China, 18: 326–336

Zhang X, Zhu Z, Zhang C, Ge Y, Zhao J, Zhang J, Nie W, Ren Q, Zhang W, Ruan H, Yang J, Wu T. 1998. Study of the crust and upper mantle structure in and around the Zhangjiakou-Bohai seismic belt (in Chinese). In: Active Fault Research: Theory and Application (6). Beijing: Seismological Press

Zhao B, Gao Y, Shi Y T. 2013. Precise relocation of small earthquakes occurred in North China and its tectonic implication (in Chinese). Earthquake, 33: 12–21

Zhao D, Mishra O P, Sanda R. 2002. Influence of fluids and magma on earthquakes: Seismological evidence. Phys Earth Planet Inter, 132: 249–267

Zhao D, Todo S, Lei J. 2005. Local earthquake reflection tomography of the Landers aftershock area. Earth Planet Sci Lett, 235: 623–631

Zhao Y L, Sun R W, Mei S R. 1993. Relocation of earthquake parameters in Bohai Sea and its adjacent areas (in Chinses). Earthq Res China, 9: 129–137

Zhu L, Kanamori H. 2000. Moho depth variation in southern California from teleseismic receiver functions. J Geophys Res, 105: 2969–2980

Zhu L P, Zeng R S, Liu F T. 1990. 3-D P-wave velocity structure of crust and upper mantle in Beijing-Tianjin-Tangshan-Zhangjiakou area (in Chinese). Chin J Geophys, 33: 267–277

(Responsible editor: Ling CHEN)